crystals

MDPI

Article

First-Principles Study of the Effects of Ti Content on Mechanical Properties and Microscopic Mechanism in $Cu_2AlMn_{1-x}Ti_x$ Alloys

Kaiyang Zheng, Shuang Xu *, Lisheng Liu and Jili Liu

Hubei Key Laboratory of Theory and Application of Advanced Materials Mechanics, Wuhan University of Technology, Wuhan 430070, China
* Correspondence: xu_shuang@whut.edu.cn

Abstract: It has been found that the addition of Ti can improve the strength of Cu-Al-Mn alloys and adjust their mechanical properties. However, the internal mechanism has not been fully understood. In order to clarify the influence of Ti content on the mechanical properties and microscopic mechanism of Cu-Al-Mn alloys, the mechanical, structural, and electronic properties of $Cu_2AlMn_{1-x}Ti_x$ (x = 0, 0.25, 0.50, 0.75, 1) alloys were studied by first-principles calculations. Results show that the substituted Ti prefers to occupy the Mn site directly due to the lower formation energy. With the increase of Ti substitution content, the $L2_1$ phase stability of the alloy improves. Moreover, the elastic modulus of the alloy increases and the anisotropy factor decreases. Further analysis shows that the proportion of antibonding states under the Fermi energy of the alloy decreases and the covalent bond is enhanced after Ti substitutes Mn, which is the main mechanism for the enhancement of stability and mechanical properties. Mulliken charges change little after Ti replaces Mn, indicating that Ti has little effect on the ionic bond strength.

Keywords: Cu-Al-Mn alloys; first-principles calculation; mechanical properties; electronic properties

Citation: Zheng, K.; Xu, S.; Liu, L.; Liu, J. First-Principles Study of the Effects of Ti Content on Mechanical Properties and Microscopic Mechanism in $Cu_2AlMn_{1-x}Ti_x$ Alloys. *Crystals* **2023**, *13*, 466. https://doi.org/10.3390/cryst13030466

Academic Editors: Xiaoqiang Liu, Mingqing Liao, Yingchun Ding, Zheng Chang, Jintong Guan, Fei Zhou and Xin Liu

Received: 23 February 2023
Revised: 3 March 2023
Accepted: 5 March 2023
Published: 8 March 2023

1. Introduction

Cu-Al-Mn alloys are widely used to produce vibration-damping components because they exhibit significant superelastic properties at room temperature and are also considered one of the most promising superelastic materials for large-scale applications due to their low manufacturing costs [1–7]. However, Cu-Al-Mn alloys have the disadvantages of low strength and high anisotropy factor, which greatly limits their extended application [7]. Experiments have shown that the superelasticity hysteresis curve of Cu-Al-Mn alloys varies significantly with crystal orientation under uniaxial stretching [8–10]. The superelastic strain of [10] crystal orientation is obviously larger than that of other crystal orientations. It is widely believed that Cu-Al-Mn alloys have obvious mechanical anisotropy, which leads to extremely strong strain incongruence during deformation and stress concentration at grain boundaries. Columnar crystal alloys with specific crystal orientations instead of common polycrystalline alloys have been proposed as an effective strategy to optimize the superelastic properties of Cu-Al-Mn alloys [11,12].

Since it is challenging to explain the internal mechanism of alloys' mechanical property change in experiments, first-principles simulation has become more popular as a useful tool [13–28]. The differential charge has shown that the significant anisotropy in the mechanical properties of Cu-Al alloys is due to the apparent directivity of the strong bonding between the nearest-neighbor Cu atoms [16]. The addition of Mn has little effect on the mechanical anisotropy of Cu-Al-based alloys because the elastic constants are not sensitive to the changes of Mn content [17]. In terms of phase stability of alloys, some studies on Hessler alloys have shown that the superelastic effect decreases with the increase of the stability of the $L2_1$ phase during tetragonal distortion [18,19]. With respect to

the electronic properties of alloys, interatomic bonding was usually used to explain the variation in mechanical properties [20,21]. For example, in Cu-Ti alloys, the atomic bonds in Cu-Ti intermetallics are mixed bonds and the covalent bond nature determines the phase stability and mechanical properties [20]. In Cu-Zn-Sb alloys, the strength of the Cu-Sb bond is stronger than that of other bonds [21].

In addition, doping certain elements (such as Ti, Ni, Zn, and Ga) to Cu-Al-Mn alloys can improve their mechanical properties [29–35]. In particular, doping Ti into Cu-Al-Mn-based alloys can improve their strength because the Ti-rich phase formed can effectively inhibit grain growth [34]. In Cu-Al-Mn-Ti alloys, the dispersive $L2_1$-Cu_2TiAl precipitates strengthen the stabilization of stress-induced 2H(γ'_1) martensite from the $L2_1$-Cu_2AlMn parent, which results in superelasticity at deformation and shape memory effect after unloading by heating [35]. It was also found that the shape memory effects of the alloys decrease with the increase of the addition of Ti when the content of Ti is over 4.6wt%. However, the internal mechanism of the effect of Ti on the mechanical properties of Cu-Al-Mn alloys has not been fully understood. In this paper, $Cu_2AlMn_{1-x}Ti_x$ (x = 0, 0.25, 0.5, 0.75, 1) alloys were selected as the research object, based on the phenomenon that Ti replaces Mn to form a new alloy phase with Cu and Al. To study the effects of Ti content on the mechanical properties and microscopic mechanism of $Cu_2AlMn_{1-x}Ti_x$ alloys, the structural, mechanical, and electronic properties were examined using the first-principles method.

2. Materials and Methods

The austenite of Cu-Al-Mn alloy is a highly ordered $L2_1$ structure that contains four types of lattice points and its chemical formula is Cu_2AlMn [22]. As shown in Figure 1, Type I and Type II are occupied by Mn and Al atoms respectively, and Type III and Type IV are occupied by Cu atoms. Each of the four types of lattice sites individually forms a face-centered cubic (FCC) lattice.

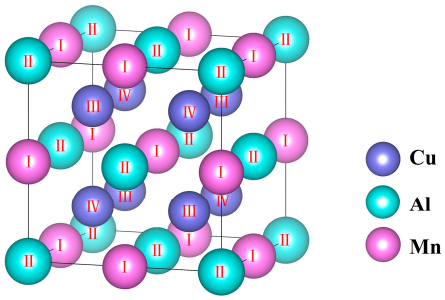

Figure 1. $L2_1$ crystal structure.

All simulations were implemented using the Vienna Ab-initio Simulation Package (VASP) [36,37] based on density functional theory. Generalized gradient approximation (GGA) [38] and Perdew-Burke-Enzerh exchange-correlation (PBE) functional [39] were used to describe the exchange-correlation potential. The projector augmented-wave (PAW) pseudopotential approach was used to describe atomic potentials [37,40]. Typical electronic configurations of Cu, Al, Mn, and Ti are $3p^63d^{10}4s^1$, $3s^23p^1$, $3p^63d^54s^2$, and $3p^63d^24s^2$, respectively. A kinetic energy cutoff of 700 eV, an energy convergence criterion of 10^{-7} eV during the electronic self-consistency loop, and a force convergence criterion of 0.005 eV/Å during the structural relaxation were adopted. The first Brillouin zone was sampled using 13 × 13 × 13 k-points in the Monkhorst-Pack scheme [41]. The lattice constant of the unit cell after relaxation is 5.933 Å, which agrees well with the experimentally measured values of 5.965 Å [42], and 5.957 Å [43].

3. Results and Discussion

3.1. Structural Properties and Phase Stability

In order to study the effects of Ti content on mechanical properties and microscopic mechanism in $Cu_2AlMn_{1-x}Ti_x$ alloys, it is necessary to determine the atom occupation

mode. All possible configurations for $Cu_2AlMn_{1-x}Ti_x$ (x = 0, 0.25, 0.5, 0.75, and 1) alloys were constructed. Figure 2 shows the configurations when x = 0.25. When Ti replaces Mn, five different structural models may exist. One of them is constructed by direct substitution, i.e., Ti is located directly at the Mn site (Figure 2b, termed as Ti_{Mn}). The other four structural models belong to the indirect substitution, including: (1) Ti is located at the Al site, and the Mn site is occupied by Al (Figure 2c, termed as $Ti_{Al}Al_{Mn}$); (2) Ti is located at the Cu site and the Mn site is occupied by Cu (Figure 2d, termed as $Ti_{Cu}Cu_{Mn}$); (3) Ti is located at the Al site, the Al is located at Cu site and Mn site is occupied by Cu (Figure 2e, termed as $Ti_{Al}Al_{Cu}Cu_{Mn}$); (4) Ti is located at Cu site, Cu is located at Al site and Mn site is occupied by Al (Figure 2f, termed as $Ti_{Cu}Cu_{Al}Al_{Mn}$). In addition, when x > 0.25, mixed substitution was also considered. Atomic positions in various structural models of $Cu_2AlMn_{1-x}Ti_x$ (x = 0.25, 0.5, 0.75, and 1) alloys were shown in Table 1. It is worth noting that all structural models are cubic except for x = 0.5 (tetragonal).

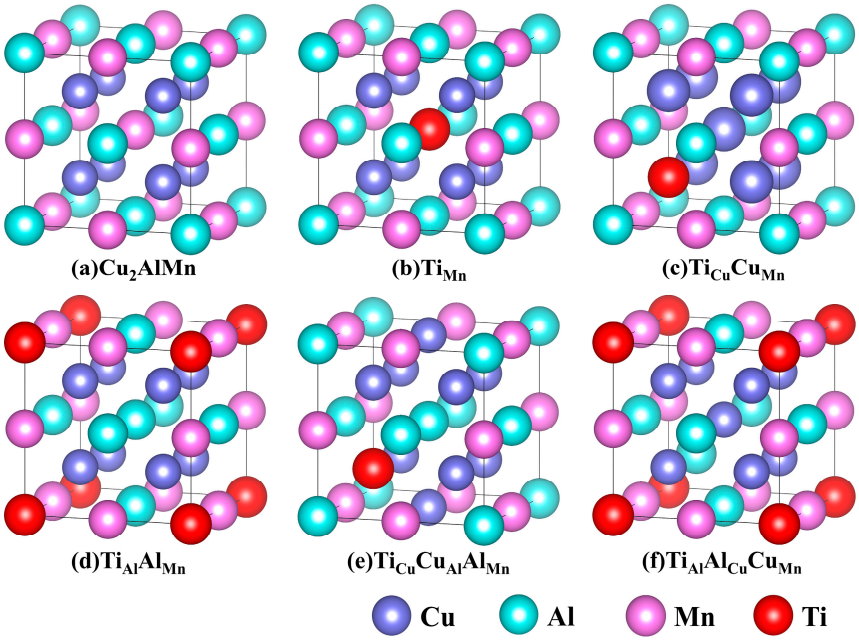

Figure 2. Different substitution manners when x = 0.25.

The formation energy (E_f) of alloys, which can be used to analyze the thermodynamic stability, was calculated by Equation (1).

$$E_f = \frac{E_{total} - N_{Cu}\mu_{Cu} - N_{Al}\mu_{Al} - N_{Mn}\mu_{Mn} - N_{Ti}\mu_{Ti}}{N_{total}} \quad (1)$$

where E_{total} represents the total ground-state energy of the unit cell, N_X (X = Cu, Al, Mn, Ti) represents the number of corresponding elements X in the cell, and μ_X (X = Cu, Al, Mn, Ti) represents the average atomic energy of the element X. The calculated formation energy was listed in Table 1. It is known that lower formation energy means that the thermodynamic stability of the compound is higher. As shown in Table 1, the configuration constructed by direct substitution always has the lowest formation energy. Therefore, the configurations constructed by direct substitution were utilized for further calculation.

To clarify the effect of Ti on phase stability, tetragonal distortion under the Bain path was applied to $L2_1$ lattices of $Cu_2AlMn_{1-x}Ti_x$ (x = 0, 0.25, 0.5, 0.75, and 1) alloys. Figure 3 displays the energy changes (E–E_0) of the $Cu_2AlMn_{1-x}Ti_x$ (x = 0, 0.25, 0.5, 0.75, and 1) alloys under different tetragonal distortions ($\Delta a/a$). The $L2_1$ phase ($\Delta a/a$ = 0) always has the lowest total energy for different substitution content of Ti, indicating that the alloys have no transition tendency to martensite. With the increase of Ti substitution content, it can be found that the energy curves near the origin become steeper, which indicates that the $L2_1$

phase stability of $Cu_2AlMn_{1-x}Ti_x$ alloys increases. This is consistent with the phenomenon that the superelastic effect properties of Cu-Al-Mn-Ti alloys start to deteriorate when the addition of Ti exceeds 4.6wt % [35].

Table 1. The formation energy of $Cu_2AlMn_{1-x}Ti_x$ alloys (x = 0, 0.25, 0.50, 0.75, and 1).

x	Occupation Manner	Atomic Site Occupation			E_f (eV/atom)
		I	II	III + IV	
0	No substitution	Mn	Al	Cu_2	–0.128
0.25	Direct substitution	$Mn_{0.75}Ti_{0.25}$	Al	Cu_2	–0.157
	Indirect substitution	$Mn_{0.75}Al_{0.25}$	$Al_{0.75}Ti_{0.25}$	Cu_2	–0.087
		$Mn_{0.75}Cu_{0.25}$	Al	$Cu_{1.75}Ti_{0.25}$	–0.114
		$Mn_{0.75}Cu_{0.25}$	$Al_{0.75}Ti_{0.25}$	$Cu_{1.75}Al_{0.25}$	–0.082
		$Mn_{0.75}Al_{0.25}$	$Al_{0.75}Cu_{0.25}$	$Cu_{1.75}Ti_{0.25}$	–0.096
0.5	Direct substitution	$Mn_{0.50}Ti_{0.50}$	Al	Cu_2	–0.197
	Indirect substitution	$Mn_{0.50}Al_{0.50}$	$Al_{0.50}Ti_{0.50}$	Cu_2	–0.122
		$Mn_{0.50}Cu_{0.50}$	Al	$Cu_{1.50}Ti_{0.50}$	–0.068
		$Mn_{0.50}Cu_{0.50}$	$Al_{0.50}Ti_{0.50}$	$Cu_{1.50}Al_{0.50}$	–0.109
		$Mn_{0.50}Al_{0.50}$	$Al_{0.50}Cu_{0.50}$	$Cu_{1.50}Ti_{0.50}$	–0.079
	Mixed substitution	$Mn_{0.50}Ti_{0.25}Al_{0.25}$	$Al_{0.75}Ti_{0.25}$	Cu_2	–0.102
		$Mn_{0.50}Ti_{0.25}Cu_{0.25}$	Al	$Cu_{1.75}Ti_{0.25}$	–0.141
0.75	Direct substitution	$Mn_{0.25}Ti_{0.75}$	Al	Cu_2	–0.247
	Indirect substitution	$Mn_{0.25}Al_{0.75}$	$Al_{0.25}Ti_{0.75}$	Cu_2	–0.180
		$Mn_{0.25}Cu_{0.75}$	Al	$Cu_{1.25}Ti_{0.75}$	–0.153
		$Mn_{0.25}Cu_{0.75}$	$Al_{0.25}Ti_{0.75}$	$Cu_{1.25}Al_{0.75}$	–0.129
		$Mn_{0.25}Al_{0.75}$	$Al_{0.25}Cu_{0.75}$	$Cu_{1.25}Ti_{0.75}$	–0.137
	Mixed substitution	$Mn_{0.25}Ti_{0.25}Al_{0.50}$	$Al_{0.50}Ti_{0.50}$	Cu_2	–0.142
		$Mn_{0.25}Ti_{0.25}Cu_{0.50}$	Al	$Cu_{1.50}Ti_{0.50}$	–0.096
		$Mn_{0.25}Ti_{0.50}Al_{0.25}$	$Al_{0.75}Ti_{0.25}$	Cu_2	–0.167
		$Mn_{0.25}Ti_{0.50}Cu_{0.25}$	Al	$Cu_{1.75}Ti_{0.25}$	–0.171
1	Direct substitution	Ti	Al	Cu_2	–0.306

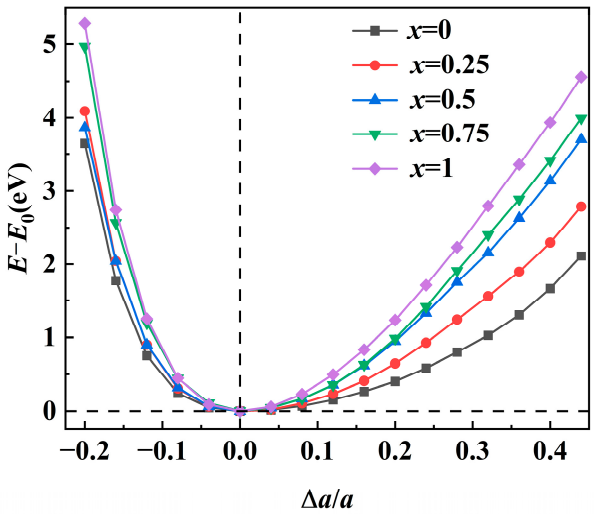

Figure 3. Variation of total energy as a function of $\Delta a/a$ in $Cu_2AlMn_{1-x}Ti_x$ (x = 0, 0.25, 0.5, 0.75, and 1). E_0 and E represent the total energy of the unit cell before and after the tetragonal distortion, respectively. $\Delta a/a$ represents the distortion rate of the lattice length.

3.2. Mechanical Properties

The elastic constants (C_{ij}) are the comprehensive representation of the elastic state and the mechanical properties of crystalline materials [28]. There are three independent

nonzero elastic constants (C_{11}, C_{12}, C_{44}) for cubic crystals and six independent nonzero elastic constants (C_{11}, C_{33}, C_{12}, C_{13}, C_{44}, C_{66}) for tetragonal crystals, which were both determined by performing six finite distortions of the lattice and deriving the elastic constants from the strain-stress relationship [44]. Table 2 shows the lattice volumes and elastic constants of $Cu_2AlMn_{1-x}Ti_x$. It is found that the calculated results in this work are in good agreement with the previous experimental and theoretical data. Based on Born stability criteria [45], for cubic crystals the elastic constants need to satisfy:

$$C_{44} > 0, C_{11} > |C_{12}|, C_{11} + 2C_{12} > 0\,, \tag{2}$$

and for tetragonal crystals the elastic constants need to satisfy [46]:

$$\begin{gathered} C_{11} > |C_{12}|,\ C_{44} > 0,\ C_{66} > 0, \\ (C_{11} + C_{12})C_{33} > 2C_{13}^2. \end{gathered} \tag{3}$$

Table 2. Lattice volumes and elastic constants of $Cu_2AlMn_{1-x}Ti_x$ (x = 0, 0.25, 0.5, 0.75, and 1).

Alloys	Source	V_0 (Å^3)	C_{11}/C_{33} (GPa)	C_{12}/C_{13} (GPa)	C_{44}/C_{66} (GPa)
Cu_2AlMn	This work.	208.83	136.94	120.40	106.15
	Experimental [47].	212.08	128.1	101.5	104.4
	Vanderbilt [17].	210.63	138.8	111.3	102.0
	FPLAPW [48].	——	137	115	112
	FPLAPW [49].	208.95	143.7	116.1	117.6
$Cu_2AlMn_{0.75}Ti_{0.25}$	This work.	212.78	144.38	120.15	101.27
$Cu_2AlMn_{0.50}Ti_{0.50}$	This work.	213.98	151.67/162.11	126.22/116.31	96.32/103.50
$Cu_2AlMn_{0.25}Ti_{0.75}$	This work.	218.02	164.65	114.06	94.14
Cu_2AlTi	This work.	219.76	178.95	115.02	101.32

All five structural models in this work satisfied the mechanical stability.

As shown in Table 2, the lattice volume increases after Ti substitute Mn, resulting in a decrease in the density. C_{11} and C_{33} are significantly higher than other elastic constants, indicating that the resistance to normal stresses of the alloys is higher. With the increase of Ti substitution content, the increase of C_{11} and C_{33} is relatively obvious, while the decrease of C_{12}, C_{13}, C_{44}, and C_{66} is relatively small. This is different from the results of the effects of Mn content on the mechanical properties of Cu-Al alloys. In Cu-Al-Mn alloys, the decrease in C_{12} value is most obvious with the change in Mn content [17]. Adding Mn can improve the stability of Cu-Al alloys, but has no significant effect on axial deformation resistance. The substitution of Mn for Ti not only improves the stability of the alloy but also improves the axial deformation resistance of the alloy.

To further investigate the elastic anisotropy of $Cu_2AlMn_{1-x}Ti_x$, a three-dimensional surface representation of the elastic anisotropy was employed to show the variation of the elastic modulus with crystal orientation. It is well known that the anisotropy of mechanical properties of materials mainly arises from the atomic regularity of the spatial arrangement. Young's modulus of arbitrary crystal orientation in cubic crystals can be expressed as [50]:

$$E_{\mathbf{n}} = \frac{1}{(S_{11} - (2S_{11} - 2S_{12} - S_{44})(l_1^2 l_2^2 + l_1^2 l_3^2 + l_2^2 l_3^2))} \tag{4}$$

Young's modulus of arbitrary crystal orientation in tetragonal crystals can be expressed as [50]:

$$E_{\mathbf{n}} = \frac{1}{(S_{11}(l_1^4 + l_2^4) + 2S_{12} l_1^2 l_2^2 + 2S_{13}(l_1^2 l_3^2 + l_2^2 l_3^2) + S_{33} l_3^4 + S_{44}(l_1^2 l_3^2 + l_2^2 l_3^2) + S_{66} l_1^2 l_2^2)} \tag{5}$$

where l_i is the cosine of the angle between the chosen direction **n** and the i-th crystal basis vector. Equations (4) and (5) displays the relationship between Young's modulus ($E_{\mathbf{n}}$) in any crystal orientation and the constants of the flexibility matrix (S_{ij}, as shown in Table 3).

Table 3. Flexibility matrix constants of $Cu_2AlMn_{1-x}Ti_x$ (x = 0, 0.25, 0.5, 0.75, and 1).

Alloys	S_{11}/S_{33} (GPa^{-1})	S_{12}/S_{13} (GPa^{-1})	S_{44}/S_{66} (GPa^{-1})
Cu_2AlMn	0.0401	−0.0187	0.0094
$Cu_2AlMn_{0.75}Ti_{0.25}$	0.0284	−0.0129	0.0099
$Cu_2AlMn_{0.50}Ti_{0.50}$	0.0242/0.0154	−0.0065/−0.0151	0.0103/0.0095
$Cu_2AlMn_{0.25}Ti_{0.75}$	0.0140	−0.0057	0.0106
Cu_2AlTi	0.0112	−0.0044	0.0099

Figure 4 shows the three-dimensional surface of Young's modulus anisotropy for different x values based on Equations (4) and (5). The crystal direction and the corresponding elastic modulus were represented by the coordinates and lengths of points on the surface, respectively. The closer the shape of the three-dimensional surface is to a sphere, the lower the anisotropy of Young's modulus is. As shown in Figure 4, with the increase of Ti substitution content, the three-dimensional surface becomes closer and closer to a sphere, which indicates that Ti substituting Mn reduces the magnitude of mechanical anisotropy of Cu_2AlMn alloy.

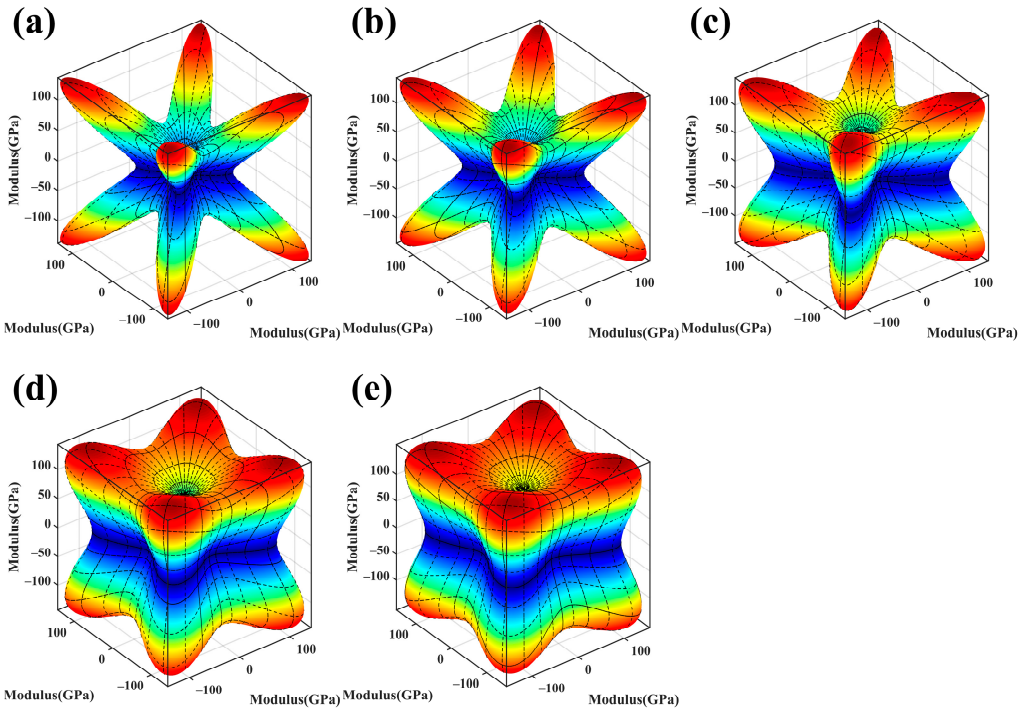

Figure 4. The three-dimensional surface of Young's modulus anisotropy: (**a**) Cu_2AlMn, (**b**) $Cu_2AlMn_{0.75}Ti_{0.25}$, (**c**) $Cu_2AlMn_{0.50}Ti_{0.50}$, (**d**) $Cu_2AlMn_{0.25}Ti_{0.75}$, and (**e**) Cu_2AlTi.

Then, in order to quantitatively understand the mechanical properties and the magnitude of anisotropy of polycrystals, the V-R-H model approximation was used to calculate the bulk modulus, shear modulus, and Young's modulus of the alloys. The V-R-H model gives the following Equations (6)–(9) [51], and the anisotropy factors of alloys were calculated by Equation (10) [16,52]. The results were shown in Table 4.

Table 4. The bulk modulus (B_H), shear modulus (G_H), Young's modulus (E), Poisson's ratio, anisotropy factor, and G/B of $Cu_2AlMn_{1-x}Ti_x$ (x = 0, 0.25, 0.5, 0.75, 1).

Alloys	B (GPa)	G (GPa)	E (GPa)	v	A_E	A_G	G/B
Cu_2AlMn	125.66	42.98	115.45	0.35	0.52	0.56	0.34
$Cu_2AlMn_{0.75}Ti_{0.25}$	128.22	45.64	122.39	0.34	0.39	0.44	0.36
$Cu_2AlMn_{0.50}Ti_{0.50}$	133.66	48.84	130.55	0.34	0.31	0.34	0.37
$Cu_2AlMn_{0.25}Ti_{0.75}$	130.92	55.90	146.63	0.31	0.17	0.19	0.43
Cu_2AlTi	136.33	63.96	166.14	0.30	0.13	0.15	0.47

Voigt and Reuss models of cubic crystals:

$$\begin{aligned} B_V &= B_R = (C_{11} + 2C_{12})/3 \\ G_V &= (C_{11} - C_{12} + 3C_{44})/5 \\ G_R &= 5(C_{11} - C_{12})C_{44}/[4C_{44} + 3(C_{11} - C_{12})] \end{aligned} \tag{6}$$

Voigt and Reuss models of tetragonal crystals:

$$\begin{aligned} M &= C_{11} + C_{12} + 2C_{33} - 4C_{13} \\ C^2 &= (C_{11} + C_{12})C_{33} - 2C_{13}^2 \\ B_V &= [2(C_{11} + C_{12}) + C_{33} + 4C_{13}]/9 \\ G_V &= (M + 3C_{11} - 3C_{12} + 12C_{44} + 6C_{66})/30 \\ B_R &= C^2/M \\ G_R &= 15\{(18B_V/C^2) + [6/(C_{11} - C_{12})] + 6/C_{44} + 3/C_{66}\}^{-1} \end{aligned} \tag{7}$$

Hill model averages Voigt and Reuss models:

$$B_H = (B_V + B_R)/2,\ G_H = (G_V + G_R)/2 \tag{8}$$

Young's modulus and Poisson's ratio are calculated by the following equation:

$$E = 9B_H G_H/(3B_H + G_H)\ ,\ v = (3B_H - 2G_H)/(6B_H + 2G_H) \tag{9}$$

The anisotropy factors of Young's modulus and shear modulus were calculated using the following equation:

$$A_E = (E_V - E_R)/(E_V + E_R)\ ,\ A_G = (G_V - G_R)/(G_V + G_R) \tag{10}$$

The results in Table 4 show that the substitution of Mn by Ti can increase the bulk modulus, shear modulus, and Young's modulus of polycrystals. When Mn is completely substituted by Ti, the shear modulus and Young's modulus of the alloys reach the highest values. This indicates that Ti substituting Mn can improve the deformation resistance of the alloy. The calculation of the mechanical anisotropy factor of the polycrystal shows that the substitution of Mn by Ti reduces the anisotropy of the alloy, which is consistent with the previous three-dimensional surface. The decrease of mechanical anisotropy can increase the strain coordination between grains with different crystal orientations during deformation and thus reduce the stress concentration at grain boundaries. In addition, the values of G/B were calculated to represent the ductility of the alloy, where the material is ductile when G/B is less than 0.5. As shown in Table 4, all alloys are ductile materials and the value of G/B of the alloys increases with the increase of x, indicating that adding Ti can make the alloy brittler.

In general, the addition of Ti can improve the deformation resistance and reduce the mechanical anisotropy of Cu_2AlMn alloys.

3.3. Density of States and Bonding Characteristics

In this section, the bonding characteristics were analyzed to examine the underlying mechanism for the change in mechanical properties.

To clarify the variation in covalent bonding, the total densities of states (TDOS) near Fermi Energy of $Cu_2AlMn_{1-x}Ti_x$ (x = 0, 0.25, 0.5, 0.75, and 1) alloys were calculated, as shown in Figure 5. At Fermi energy, there is a sufficient density of states for all systems with different x values, which indicates that compounds are metallic in nature. In spin-down TDOS, the distribution of peaks is essentially unchanged with the increase of x. However, in spin-up TDOS, the peak between −2.50 and −1.50 eV gradually disappears with the increase of x, while a new peak is generated between 0.50 and 1.12 eV. To further understand the bonding properties, the crystal orbital Hamiltonian population (COHP) analysis method [53–55] was employed to determine the bonding characteristics. The −COHP values for the interactions of all the first and second nearest neighbor atomic pairs in a unit cell were calculated, and the average −COHP values were used to represent the covalent bonding characteristic of the entire structure (Figure 6). As shown in Figure 6, the spin-up −COHP peaks between −2.50 and −1.50 eV are antibonding states, which decrease continuously as the proportion of Ti increases. However, there is no significant change in the spin-down −COHP curve in Figure 6. This indicates that the decrease of spin-up TDOS peaks between −2.50 and −1.50 eV reduces the proportion of antibonding states below Fermi energy, which makes the alloy more stable and difficult to undergo a phase transition. This may be the reason for the addition of excess Ti weakening the superelastic strain of Cu-Al-Mn-Ti alloys. Specifically, the negative Integrated COHP Values at the Fermi Level were calculated to evaluate the strength of different bonds (Listed in Table 5). As shown in Table 5, the covalent bond strength between the same atomic pairs in $Cu_2AlMn_{1-x}Ti_x$ alloys changes little under different Ti substitution content. The strength of Ti-Al and Ti-Cu bonds is stronger than that of Mn-Al and Mn-Cu bonds, which causes the increase of Young's modulus. Compared to other bonds, the strength of the Cu-Cu bond is very weak and contributes little to the covalent bonding of alloys.

Table 5. Negative integrated COHP values at the Fermi Level for $Cu_2AlMn_{1-x}Ti_x$ (x = 0, 0.25, 0.5, 0.75, and 1).

Alloys	Bond					
	Mn-Al	Mn-Cu	Al-Cu	Cu-Cu	Ti-Al	Ti-Cu
Cu_2AlMn	0.649	0.351	0.918	0.051		
$Cu_2AlMn_{0.75}Ti_{0.25}$	0.614	0.35	0.837	0.047	0.924	0.526
$Cu_2AlMn_{0.50}Ti_{0.50}$	0.607	0.349	0.804	0.044	0.964	0.528
$Cu_2AlMn_{0.25}Ti_{0.75}$	0.577	0.357	0.831	0.036	0.955	0.529
Cu_2AlTi			0.821	0.032	0.954	0.535

Then, the variation of covalent bonding strength during tetragonal distortion was examined. Figure 7 displays the electron localization function (ELF) maps of Cu_2AlMn and Cu_2AlTi for tetragonal distortion at different levels. Larger ELF values imply stronger covalent bonds, and these regions are marked in red in Figure 7. As shown in Figure 7, the ELF values between Mn and Al as well as those between Ti and Al decrease rapidly with the increase of tetragonal distortion, which indicates that the covalent bond strength of Al-Mn and Al-Ti is very sensitive to the tetragonal distortion. In order to quantitatively analyze the change of covalent bonding, the −COHP values of Cu-Mn, Cu-Al, Cu-Ti, Al-Mn, Al-Ti, and Cu-Cu bonds were integrated at Fermi energy, as shown in Figure 8. The strength of Al-Mn and Al-Ti covalent bonds declines rapidly in the early stage of the tetragonal distortion process, which is consistent with the previous analysis. However, the strength of Cu-Mn, Cu-Al, and Cu-Ti covalent bonds changes relatively slowly and the strength of Cu-Cu covalent bonds is always very weak. The result indicates that the strength of Al-Mn and Al-Ti covalent bonds is unstable and greatly affected by tetragonal distortion.

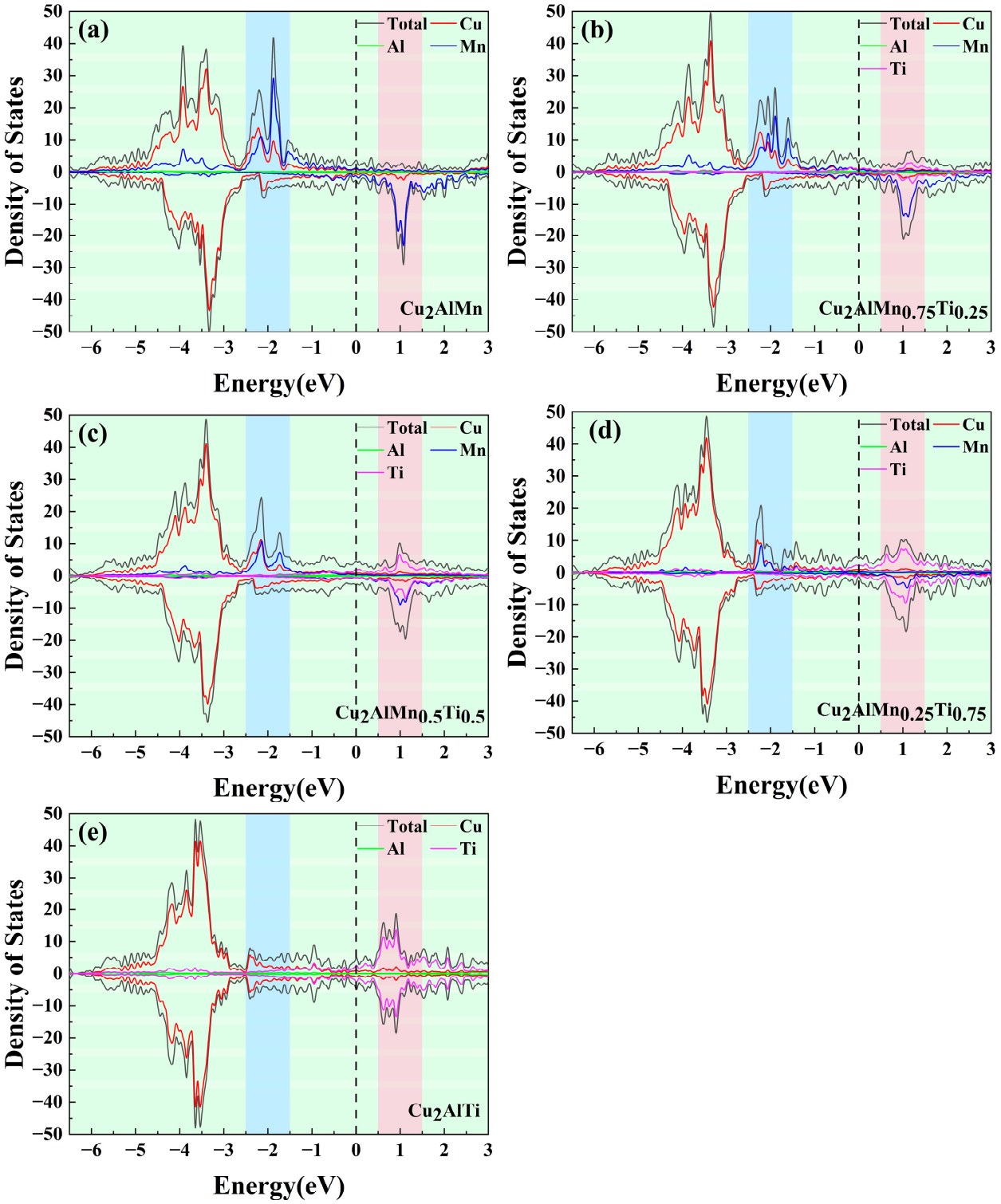

Figure 5. The TDOS of $Cu_2AlMn_{1-x}Ti_x$ (x = 0, 0.25, 0.5, 0.75, and 1) near Fermi Energy: (**a**) Cu_2AlMn, (**b**) $Cu_2AlMn_{0.75}Ti_{0.25}$, (**c**) $Cu_2AlMn_{0.50}Ti_{0.50}$, (**d**) $Cu_2AlMn_{0.25}Ti_{0.75}$, and (**e**) Cu_2AlTi. The blue regions indicate that TDOS significantly decreases with the increase of Ti content. The red regions indicate that TDOS significantly increases with the increase of Ti content.

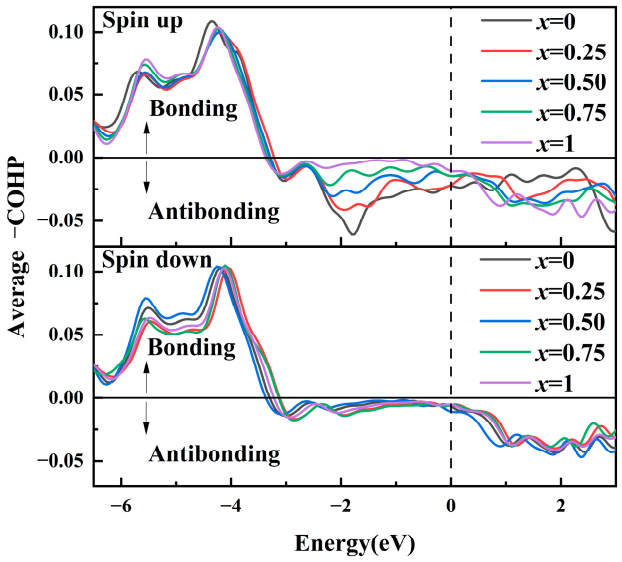

Figure 6. The average –COHP values of $Cu_2AlMn_{1-x}Ti_x$ (x = 0, 0.25, 0.5, 0.75, and 1) unit cell near Fermi Energy.

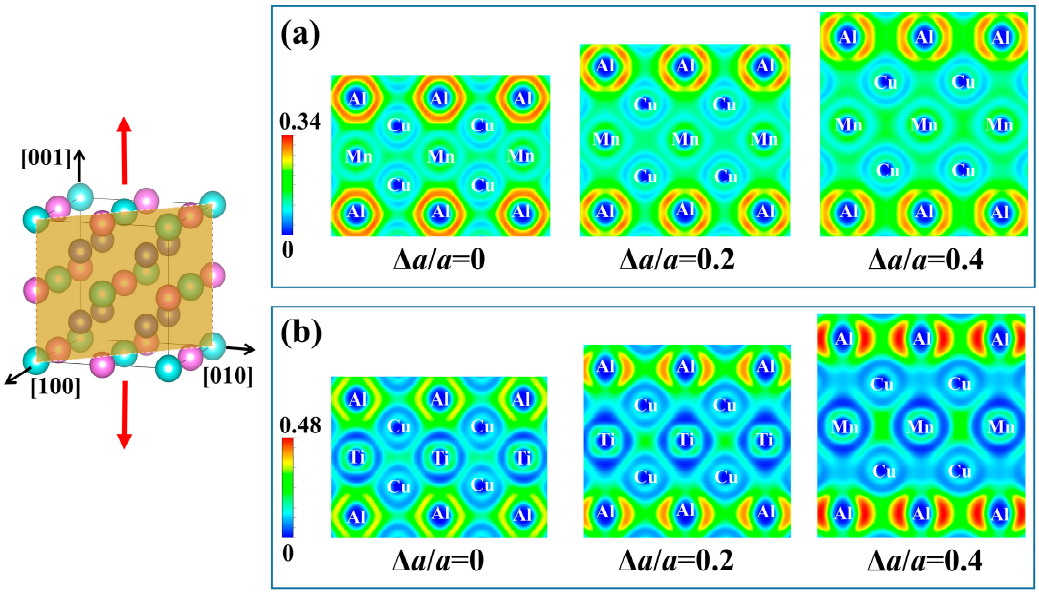

Figure 7. The ELF map of alloys in (110) crystal face: (**a**) Cu_2AlMn, (**b**) Cu_2AlTi. A larger ELF value indicates a relatively higher degree of localization of the electron.

In addition, the ionic bonding properties of $Cu_2AlMn_{1-x}Ti_x$ alloys were also investigated. Mulliken population analysis [56] results were used to analyze electronic transfer information between different atoms, as shown in Table 6. In $Cu_2AlMn_{1-x}Ti_x$ alloys, Cu, Mn, and Ti are the elements that lose electrons while Al is the element that gains electrons, which indicates the ionic nature of alloys. As the Ti substitution content increases, there is no significant change in the number of electrons from Cu and Mn to Al. The ionic bonding strength between Cu, Mn, and Al is insensitive to the Ti element.

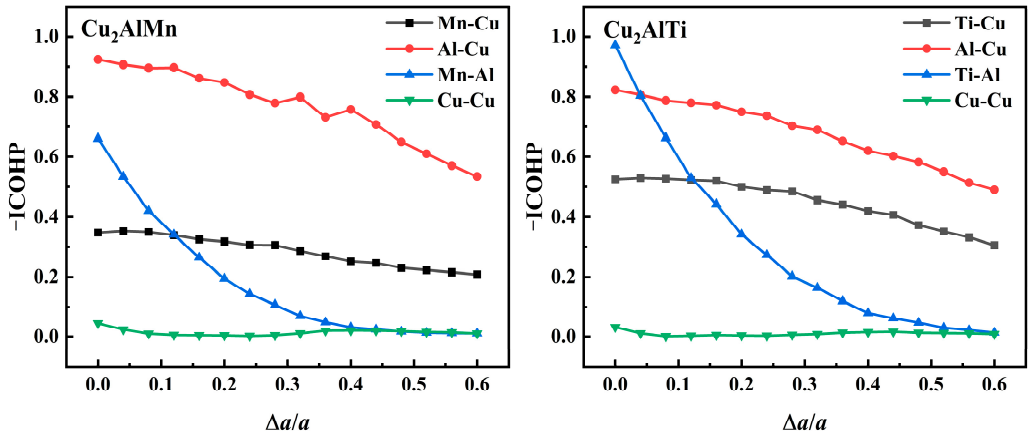

Figure 8. Negative Integrated COHP Values at the Fermi Level for Cu_2AlMn and Cu_2AlTi during the tensile process.

Table 6. Atomic Mulliken charge of $Cu_2AlMn_{1-x}Ti_x$ (x = 0, 0.25, 0.5, 0.75, and 1).

Alloys	Elements	*s*	*p*	*d*	Total	Charge (*e*)
Cu_2AlMn	Cu	0.96	6.00	9.68	16.64	+0.36
	Al	1.14	3.20		4.34	−1.34
	Mn	0.76	6.00	5.62	12.38	+0.62
$Cu_2AlMn_{0.75}Ti_{0.25}$	Cu	0.97	6.00	9.67	16.64	+0.36
	Al-I (0.25)	1.14	3.27		4.41	−1.41
	Al-II (0.75)	1.14	3.17		4.31	−1.31
	Mn	0.76	6.00	5.61	12.37	+0.63
	Ti	0.71	6.00	2.71	9.42	+0.58
$Cu_2AlMn_{0.5}Ti_{0.5}$	Cu	0.97	6.00	9.67	16.64	+0.36
	Al-I (0.50)	1.14	3.23		4.37	−1.37
	Al-II (0.50)	1.14	3.15		4.29	−1.29
	Mn	0.76	6.00	5.59	12.35	+0.65
	Ti	0.72	6.00	2.70	9.42	+0.58
$Cu_2AlMn_{0.25}Ti_{0.75}$	Cu	0.97	6.00	9.66	16.63	+0.37
	Al-I (0.75)	1.14	3.19		4.33	−1.33
	Al-II (0.25)	1.14	3.16		4.30	−1.30
	Mn	0.74	6.00	5.58	12.32	+0.68
	Ti	0.71	6.00	2.73	9.44	+0.56
Cu_2AlTi	Cu	0.97	6.00	9.65	16.62	+0.38
	Al	1.14	3.19		4.33	−1.33
	Ti	0.72	6.00	2.71	9.43	+0.57

4. Conclusions

In this paper, the effect of Ti replacing Mn on the mechanical properties of $Cu_2AlMn_{1-x}Ti_x$ (x = 0, 0.25, 0.5, 0.75, and 1) alloys were studied by the first-principles method, and the internal mechanism was analyzed from the perspective of structural and electronic properties. The following conclusions could be summarized:

(1) In terms of mechanical properties, all of the $Cu_2AlMn_{1-x}Ti_x$ alloys presented in this work are mechanically stable. With the increase of x, Young's modulus, shear modulus, and volume modulus increase, and the mechanical anisotropy factor decreases, which indicates that the addition of Ti improves the mechanical properties of the alloy.

(2) In terms of structural properties and phase stability, Ti atoms prefer to occupy the position of Mn atoms directly in $Cu_2AlMn_{1-x}Ti_x$ alloys, and the $L2_1$ phase is the most stable phase in the process of tetragonal distortion. With the increase of Ti substitution content, the phase stability of the alloy improves.

(3) In terms of microscopic mechanism, the proportion of antibonding states under the Fermi energy of $Cu_2AlMn_{1-x}Ti_x$ alloys decreases with the increase of Ti substitution content, which is the main reason for the increase in stability and mechanical properties. The strength of Ti-Al and Ti-Cu bonds is stronger than that of Mn-Al and Mn-Cu bonds. In particular, the covalent bond strength of Al-Mn and Al-Ti is relatively sensitive to tetragonal distortion. In addition, the addition of Ti has little effect on the ionic bond strength of Cu_2AlMn alloy.

Author Contributions: K.Z. carried out the calculations and wrote the original draft preparation. S.X. conceived and designed the whole process of the investigation. S.X., L.L. and J.L. contributed to data analysis. All authors contributed to discussion, paper writing and revising. All authors have read and agreed to the published version of the manuscript.

Funding: This research was funded by the National Natural Science Foundation of China (11402183, 51604206, and 51974217), and National Defense Science and technology foundation strengthening program. Shuang Xu was supported by China Scholarship Council No. 201906955063.

Data Availability Statement: Data sharing is not applicable to this article.

Conflicts of Interest: The authors declare no conflict of interest.

References

1. Huang, H.; Wang, W.; Liu, J.; Xie, J. Progress on the Applications of Cu-Based Shape Memory Alloys. *Mater. Chin.* **2016**, *35*, 12.
2. Lu, X.; Chen, F.; Li, W.; Zheng, Y. Effect of Ce addition on the microstructure and damping properties of Cu-Al-Mn shape memory alloys. *J. Alloy. Compd.* **2009**, *480*, 608–611. [CrossRef]
3. Ozbulut, O.E.; Hurlebaus, S.; Desroches, A.R. Seismic response control using shape memory alloys: A review. *J. Intell. Mater. Syst. Struct.* **2011**, *22*, 1531–1549. [CrossRef]
4. Zhang, Z.; Bi, K.; Hao, H.; Sheng, P.; Xiao, D. Development of a novel deformation-amplified shape memory alloy-friction damper for mitigating seismic responses of RC frame buildings. *Eng. Struct.* **2020**, *216*, 110751. [CrossRef]
5. Varughese, K.; El-Hacha, R. Design and behaviour of steel braced frame reinforced with NiTi SMA wires. *Eng. Struct.* **2020**, *212*, 110502. [CrossRef]
6. Rodrigue, H.; Wang, W.; Bhandari, B.; Han, M.W.; Ahn, S.H. SMA-based smart soft composite structure capable of multiple modes of actuation. *Compos. Part B-Eng.* **2015**, *82*, 152–158. [CrossRef]
7. Huang, H.; Wang, W.; Liu, J.; Xie, J. Progress on Microstructure Design of High Performance Cu-Based Shape Memory Alloys. *Mater. Chin.* **2016**, *35*, 835–842.
8. Omori, T.; Koeda, N.; Sutou, Y.; Kainuma, R.; Ishida, K. Superplasticity of Cu-Al-Mn-Ni shape memory alloy. *Mater. Trans.* **2007**, *48*, 2914–2918. [CrossRef]
9. Sutou, Y.; Omori, T.; Wang, J.J.; Kainuma, R.; Ishida, K. Characteristics of Cu-Al-Mn-based shape memory alloys and their applications. *Mater. Sci. Eng. A-Struct.* **2004**, *378*, 278–282. [CrossRef]
10. Sutou, Y.; Omori, T.; Kainuma, R. Grain size dependence of pseudoelasticity in polycrystalline Cu-Al-Mn-based shape memory sheets. *Acta Mater.* **2013**, *61*, 3842–3850. [CrossRef]
11. Liu, J.; Huang, H.; Xie, J. Superelastic anisotropy characteristics of columnar-grained Cu-Al-Mn shape memory alloys and its potential applications. *Mater. Des.* **2015**, *85*, 211–220. [CrossRef]
12. Xie, J.; Liu, J.; Huang, H. Structure design of high-performance Cu-based shape memory alloys. *Rare Met.* **2015**, *34*, 607–624. [CrossRef]
13. Wang, S.; Fan, C. Crystal structures of Al_2Cu revisited: Understanding existing phases and exploring other potential phases. *Metals* **2019**, *9*, 1037. [CrossRef]
14. Cheng, J.; Yun, Y.; Wang, J.; Rui, J.; Wang, S.; Du, Y. Effect of Nb on the Microstructure and Mechanical Properties of Ti_2Cu Intermetallic through the First-Principle Calculations and Experimental Investigation. *Metals* **2020**, *10*, 547. [CrossRef]
15. Bu, Y.; Peng, S.; Wu, S.; Wei, Y.; Wang, G.; Liu, J.; Wang, H. Unconventional deformation behaviours of nanoscaled high-entropy alloys. *Entropy* **2018**, *20*, 778. [CrossRef]
16. Zhou, W.; Liu, L.; Li, B.; Song, Q.; Wu, P. Structural; elastic; and electronic properties of al-cu intermetallics from first-principles calculations. *J. Electron. Mater.* **2018**, *38*, 356–364. [CrossRef]
17. Alés, A.; Lanzini, F. Mechanical and thermodynamical properties of β Cu-Al-Mn alloys along the Cu_3Al-Cu_2AlMn compositional line. *Solid State Commun.* **2020**, *319*, 113980. [CrossRef]
18. Yan, H.; Liu, H.; Huang, X.; Zhang, M.; Jia, N.; Bai, J. First-principles investigation of mg substitution for ga on martensitic transformation; magnetism and electronic structures in Ni_2MnGa. *J. Alloy. Compd.* **2020**, *843*, 156049. [CrossRef]

19. Liang, X.; Bai, J.; Guan, Z.; Gu, J.; Yan, H.; Zhang, Y.; Esling, C.; Zhao, X.; Zuo, L. Revealing the role of site occupation in phase stability;magnetic and electronic properties of Ni-Mn-In alloys by ab initio approach. *J. Mater. Sci. Technol.* **2021**, *83*, 90–101. [CrossRef]
20. Zhu, Y.; Yan, M.; Zhang, Y.; Zhang, C. First-principles investigation of structural; mechanical and electronic properties for Cu-Ti intermetallics. *Comput. Mater. Sci.* **2016**, *123*, 70–78. [CrossRef]
21. Samiran, M.; Biplab, K.; Swastika, C.; Jana, P. Atomic Ordering of Two Neighboring Transition Metals Cu and Zn from Binary CuZn to Ternary Cu_3ZnSb. *J. Partha Inorg. Chem.* **2018**, *57*, 11970–11977.
22. Lanzini, F.; Alés, A. The role of magnetism in the formation of the two-phase miscibility gap in β Cu–Al–Mn. *J. Magn. Magn. Mater.* **2015**, *395*, 234–239. [CrossRef]
23. Li, J.; Xu, S.; Zhang, J.; Liu, L. First-Principles Predicting Improved Ductility of Boron Carbide through Element Doping. *J. Phys. Chem. C* **2021**, *125*, 11591–11603. [CrossRef]
24. Li, J.; Liu, L.; Xu, S.; Zhang, J. Mechanical; electronic properties and deformation mechanisms of Ti_3B_4 under uniaxial compressions: A first-principles calculation. *Acta Phys. Sin-Ch. Ed.* **2020**, *69*, 043102. [CrossRef]
25. Li, J.; An, Q.; Liu, L. Local amorphization in boron carbide at finite temperature: Strategies toward improved ductility. *Phys. Rev. B* **2021**, *104*, 134105. [CrossRef]
26. Li, J.; Liu, L.; Xu, S.; Zhang, J.; Wu, Y. The effects of carbon content on the anisotropic deformation mechanism of boron carbide. *Materials* **2018**, *11*, 1861. [CrossRef]
27. Li, J.; Xu, S.; Liu, L.; Zhen, W.; Zhang, J.; Liu, Q. Mechanism for amorphization of boron carbide under complex stress conditions. *Mater. Res. Express* **2018**, *5*, 055204. [CrossRef]
28. Li, J.; Liu, L.; Xu, S.; Zhang, J.; She, W. First-principles study of mechanical, electronic properties and anisotropic deformation mechanisms of TiB under uniaxial compressions. *Appl. Phys. A* **2019**, *125*, 222. [CrossRef]
29. Yang, S.; Hong, S.; Li, M.; Qing, X.; Guo, L.; Guo, Y.; Wang, C.; Liu, X. Microstructure; martensitic transformation and shape memory effect of polycrystalline Cu-Al-Mn-Fe alloys. *Sci. China Technol. Sci.* **2021**, *64*, 400–406. [CrossRef]
30. Brazolin, G.; Silva, C.; Silva, L.; Silva, R. Phase transformations in an annealed Cu-9Al-10Mn-3Gd alloy. *J. Therm. Anal. Calorim.* **2018**, *134*, 1405–1412. [CrossRef]
31. Yang, Q.; Yin, D.; Ge, J.; Chen, J.; Wang, S.; Peng, H.; Wen, Y. Suppressing heating rate-dependent martensitic stabilization in ductile Cu-Al-Mn shape memory alloys by Ni addition: An experimental and first-principles study. *Mater. Charact.* **2018**, *145*, 381–388. [CrossRef]
32. Manasijevic, D.; Grguri, T.; Balanovic, L.; Stamenkovi, U.; Gorgievski, M. Effect of Mn content on the microstructure and phase transformation temperatures of the Cu-Al-Mn-Ag shape memory alloys. *Kovove Mater.* **2020**, *58*, 293–299. [CrossRef]
33. Yang, L.; Jiang, X.; Sun, H.; Shao, Z.; Fang, Y.; Shu, R. Effect of Ta addition on microstructures; mechanical and damping properties of Cu-Al-Mn-Ti alloy. *J. Mater. Res. Technol.* **2021**, *15*, 3825–3835. [CrossRef]
34. Dalvand, P.; Raygan, S.; López, G.A.; Meléndez, M.B.; Chernenko, V.A. Properties of rare earth added Cu-12wt%Al-3wt%Ni-0.6wt%Ti high temperature shape memory alloy. *Mater. Sci. Eng.* **2019**, *754*, 370–381. [CrossRef]
35. Chen, X.; Zhang, F.; Chi, M.; Yang, S.; Wang, C.; Liu, X. Microstructure; superelasticity and shape memory effect by stress-induced martensite stabilization in Cu-Al-Mn-Ti shape memory alloys. *Mater. Sci. Eng.* **2018**, *236*, 10–17. [CrossRef]
36. Kresse, G.; Furthmüller, J. Efficiency of ab-initio total energy calculations for metals and semiconductors using a plane-wave basis set. *Comput. Mater. Sci.* **1996**, *6*, 15–50. [CrossRef]
37. Kresse, G.; Furthmüller, J. Efficient iterative schemes for ab initio total-energy calculations using a plane-wave basis set. *Phys. Rev. B* **1996**, *54*, 11169. [CrossRef]
38. Perdew, J.P.; Burke, K.; Ernzerhof, M. Generalized gradient approximation made simple. *Phys. Rev. Lett.* **1996**, *77*, 3865–3869. [CrossRef]
39. Perdew, J.P.; Ernzerhof, M.; Burke, K. Rationale for mixing exact exchange with density functional approximations. *J. Chem. Phys.* **1996**, *105*, 9982–9985. [CrossRef]
40. Kresse, G.; Joubert, D. From ultrasoft pseudopotentials to the projector augmented-wave method. *Phys. Rev. B* **1999**, *59*, 1758–1775. [CrossRef]
41. Monkhorst, H.J.; Pack, J.D. Special points for Brillouin-zone integrations. *Phys. Rev. B* **1976**, *13*, 5188–5192. [CrossRef]
42. Kainuma, R.; Saloh, N.; Liu, X.J.; Ohnuma, I.; Ishida, K. Phase equilibria and Heusler phase stability in the Cu-rich portion of the Cu-Al-Mn system. *J. Alloy. Compd.* **1998**, *266*, 191–200. [CrossRef]
43. Soltys, J. X-ray diffraction research of the order-disorder transitions in the ternary Heusler alloys B_2MnAl (B= Cu, Ni, Co, Pd, Pt). *Phys. Status Solidi A* **1981**, *66*, 485–491. [CrossRef]
44. Page, Y.L.; Saxe, P. Symmetry-General Least-Squares Extraction of Elastic Data for Strained Materials From ab Initio Calculations of Stress. *Phys. Rev. B* **2002**, *65*, 104104. [CrossRef]
45. Born, M. On the stability of crystal lattices. I. *Math. Proc. Camb. Philos. Soc.* **1940**, *36*, 160–172. [CrossRef]
46. Mouhat, F.; Coudert, F.X. Necessary and Sufficient Elastic Stability Conditions in Various Crystal Systems. *Phys. Rev. B* **2014**, *90*, 224104. [CrossRef]
47. Michelutti, B.; Bathie, R.; Lacheisserie, E.; Waintal, A. Magnetization; magnetocrystalline anisotropy; magnetostriction and elastic constants of the heusler alloy: Cu_2MnAl. *Solid State Commun.* **1978**, *25*, 163–168. [CrossRef]

48. Jalilian, J. Comment on study of electronic; magnetic; optical and elastic properties of Cu_2MnAl a gapless full heusler compound. *J. Alloy. Compd.* **2014**, *12*, 039. [CrossRef]
49. Wu, S.C.; Naghavi, S.S.; Fecher, G.H.; Felser, C. Elastic properties and stability of Heusler compounds: Cubic Co2YZ compounds with $L2_1$ structure. *J. Appl. Phys.* **2019**, *125*, 082523. [CrossRef]
50. Nye, J.F. *Physical Properties of Crystals*; Oxford University Press: Oxford, UK, 1985; pp. 143–145.
51. Hill, R.J. Elastic properties of reinforced solids: Some theoretical principles. *J. Mech. Phys. Solids* **1963**, *11*, 357–372. [CrossRef]
52. Chung, D.H.; Buessem, W.R. The elastic anisotropy of crystals. *J. Appl. Phys.* **1967**, *38*, 2010–2012. [CrossRef]
53. Maintz, S. LOBSTER: A tool to extract chemical bonding from plane-wave based DFT. *J. Comput. Chem.* **2016**, *37*, 1030–1035. [CrossRef]
54. Dronskowski, R.; Bloechl, P.E. Crystal orbital Hamilton populations (COHP): Energy-resolved visualization of chemical bonding in solids based on density-functional calculations. *J. Phys. Chem. B* **1993**, *97*, 8617–8624. [CrossRef]
55. Burdett, J.K.; Mccormick, T.A. Electron localization in molecules and solids: The meaning of ELF. *J. Phys. Chem. A* **1998**, *102*, 91–96. [CrossRef]
56. Mulliken, R.S. Molecular Compounds and their Spectra. III. The Interaction of Electron Donors and Acceptors. *J. Phys. Chem.* **1952**, *56*, 801–822. [CrossRef]